

Nanocomposite Membranes Enhance Bone Regeneration Through Restoring Physiological Electric Microenvironment

Xuehui Zhang,^{†,‡,¶,||} Chenguang Zhang,[‡] Yuanhua Lin,[§] Penghao Hu,^{||} Yang Shen,[§] Ke Wang,[§] Song Meng,[⊥] Yuan Chai,^{†,‡} Xiaohan Dai,[⊥] Xing Liu,[⊥] Yun Liu,[⊥] Xiaoju Mo,[⊥] Cen Cao,[‡] Shue Li,[‡] Xuliang Deng,^{*,⊥,†,‡,¶,||} and Lili Chen^{*,‡}

[†]Department of Dental Materials, Peking University School and Hospital of Stomatology, Beijing 100081, PR China

[‡]Department of Stomatology, Union Hospital, Tongji Medical College, Huazhong University of Science and Technology, Wuhan, Hubei 430022, PR China

[§]State Key Laboratory of New Ceramics and Fine Processing, and Department of Materials Science and Engineering, Tsinghua University, Beijing 100084, PR China

^{||}Department of Polymer Science & Engineering, School of Chemistry & Biological Engineering, University of Science & Technology Beijing, Beijing 100083, China

[⊥]Department of Geriatric Dentistry, Peking University School and Hospital of Stomatology, Beijing 100081, PR China

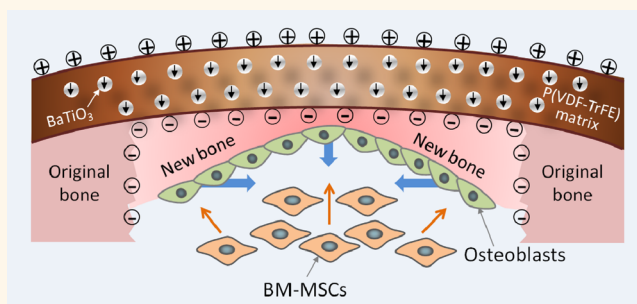
[¶]National Engineering Laboratory for Digital and Material Technology of Stomatology, Beijing 100081, PR China

^{||}Beijing Laboratory of Biomedical Materials, Peking University School and Hospital of Stomatology, Beijing 100081, PR China

S Supporting Information

ABSTRACT: Physiological electric potential is well-known for its indispensable role in maintaining bone volume and quality. Although implanted biomaterials simulating structural, morphological, mechanical, and chemical properties of natural tissue or organ has been introduced in the field of bone regeneration, the concept of restoring physiological electric microenvironment remains ignored in biomaterials design. In this work, a flexible nanocomposite membrane mimicking the endogenous electric potential is fabricated to explore its bone defect repair efficiency. BaTiO₃ nanoparticles (BTO NPs) were first coated with polydopamine. Then the composite membranes are fabricated with homogeneous distribution of Dopa@BTO NPs in poly(vinylidene fluoride-trifluoroethylene) (P(VDF-TrFE)) matrix. The surface potential of the nanocomposite membranes could be tuned up to -76.8 mV by optimizing the composition ratio and corona poling treatment, which conform to the level of endogenous biopotential. Remarkably, the surface potential of polarized nanocomposite membranes exhibited a dramatic stability with more than half of original surface potential remained up to 12 weeks in the condition of bone defect. *In vitro*, the membranes encouraged bone marrow mesenchymal stem cells (BM-MSCs) activity and osteogenic differentiation. *In vivo*, the membranes sustainably maintained the electric microenvironment giving rise to rapid bone regeneration and complete mature bone-structure formation. Our findings evidence that physiological electric potential repair should be paid sufficient attention in biomaterials design, and this concept might provide an innovative and well-suited strategy for bone regenerative therapies.

KEYWORDS: physiological electric potential, nanocomposite membranes, ferroelectricity, polarization, bone regeneration



Nature might give us inspiration for designing and fabricating biomimetic materials to obtain the desired tissue regeneration outcome. Electrical signals are present in all functions of living cells and organisms.^{1,2} Physiological endogenous electric fields or electric potential exist in the injured tissue and have been proposed to be important in wound healing.^{3,4} Electrical current or electric

potential of native bone and periosteum exists and plays an indispensable role in maintaining bone volume and quality.⁵⁻⁷ In small bone defects, spontaneous fast bone regeneration and

Received: April 2, 2016

Accepted: July 7, 2016

Published: July 7, 2016

complete biological repair can be expected,⁸ while in large bone defects, for example, critical-sized bone defect, delayed and compromised healing often occurs.⁹ Spontaneous fast bone regeneration might be due to rapid formation of periosteum-like tissue, which can give rise to quick rehabilitation of the electric microenvironment in small bone defect, while in large bone defects, it takes more time for the periosteum-like tissue to migrate across the defect, which will lead to delayed rehabilitation of the local electrical environment. Fibrous and epithelial tissue then migrates into the defect area, which might compromise the rate, quality, and efficacy of bone healing.¹⁰ It has been proposed that wound electric microenvironment repair should be a prime directional cue for improved bone regeneration. These considerations should shed light on designing innovative implant biomembranes with inherent electrical activity mimicking physiological electrical properties. More effective strategies might be achieved for bone regeneration through recovering destroyed physiological potential microenvironment.¹¹

Therefore, in this work, the conceptual proof research on bone defect repair mediated by ferroelectric composite membranes with biomimetic electric microenvironment is presented. The nanocomposite membranes were fabricated with homogeneous distribution of ferroelectric BaTiO₃ nanoparticles (BTO NPs) in poly(vinylidene fluoridetrifluoroethylene) (P(VDF-TrFE)) matrix. As described in Figure 1, electrical dipoles of BTO NPs are

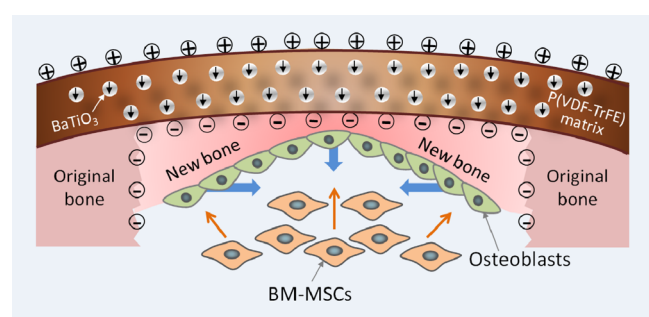


Figure 1. Illustration of biomimetic electric microenvironment created by BTO NP/P(VDF-TrFE) composite membranes encouraging bone defect repair. Electrical dipoles of BTO NPs are reoriented in the direction of poling electric field after corona poling treatment, and consequently induced charges are generated on the outer surface of the membrane. When the composite membranes are implanted like native periosteum covering the bone defect, endogenous bone marrow mesenchymal stem cells (BM-MSCs) can be recruited by galvanotaxis and induced to differentiate into osteoblasts. Consequently, the membranes sustainably maintained electric microenvironment giving rise to rapid bone regeneration and complete mature bone-structure formation integrated with original bone. The short black arrows denote the direction of electrical dipole in BTO NPs. The blue thick arrows denote the direction of new bone growth. The orange thin arrows denote the recruitment and osteogenic differentiation of BM-MSCs.

reoriented in the direction of poling electric field after corona poling treatment, and consequently opposite charges are generated in the inner sides of membranes. In order to maintain electric balance of the material system, corresponding offset charges will present on the outer surface of the membranes. When the nanocomposite membranes are implanted like native periosteum covering the bone defect area, endogenous bone marrow mesenchymal stem cells (BM-MSCs) can be recruited by galvanotaxis and induced to differentiate into osteoblasts

by the biopotential mimicking microenvironment created by nanocomposite membranes. The surface potential of polarized nanocomposite membranes exhibited dramatic stability with more than half of the original surface potential remained up to 12 weeks when implanted in bone defects. Consequently, the membranes sustainably maintained electric microenvironment giving rise to rapid bone regeneration and complete defect repair with mature bone-structure formation integrated with original bone.

RESULTS AND DISCUSSION

We utilized a solution casting method to fabricate BTO NP/P(VDF-TrFE) composite membranes (Figure 2a). The pure phase of BTO NPs was evidenced by the X-ray diffraction patterns (Figure S1a). The surfaces of BTO NPs were modified with polydopamine to prevent aggregation in the polymer matrix. The thin amorphous coating of ~5 nm could be observed on the surface of BTO NPs (Figure S1b). The amorphous coating was further identified as polydopamine layers by the much increased signal from N 1s electrons in dopamine in the XPS spectra (Figure S1c). Due to the shielding by the polydopamine coatings on the surfaces of BTO NPs, XPS signals of Ba 3d and Ti 2p electrons from BTO NPs were much reduced (Figure S1c). By introducing polydopamine surface layers on BTO NPs, better interface compatibility between the BTO NPs fillers and P(VDF-TrFE) matrix was achieved, resulting in homogeneous dispersion of polydopamine@BTO NPs in the membranes (Figure 2b and Figure S2d). The presence of BTO NPs in the P(VDF-TrFE) matrix was further confirmed by EDS spectra (Figure S2e). The polydopamine coating on the BTO NPs not only acts as surfactant but also has been found to be an extremely versatile platform for secondary reactions with organic species, giving rise to organic ad-layers or matrix covalently bonded with the nanofillers.¹²

By tuning the content of BTO NPs, we fabricated a set of membranes (0, 1, 3, and 5 vol % BTO) with average thickness of 50–60 μm (Figure S2a,c). When the concentration of BTO NP fillers was increased to 10 vol %, microcracks appeared between the fillers and polymer matrix (data not shown). Taking advantage of the inherent elastic property of P(VDF-TrFE) and the excellent compatibility between the nanofillers and the polymer matrix, these nanocomposite membranes exhibited excellent flexibility (Figure 2c), which makes them adaptable to clinical manipulation.

The surface properties of BTO NP/P(VDF-TrFE) membranes were investigated. The surface morphology and homogeneous dispersion of BTO NPs in membranes were not undermined by corona poling treatment at room temperature (Figure S2b). AFM analysis showed that all membranes had nanoscale surface roughness with slight BTO NP-content dependence (Figure S3a,b). The surface wettability showed that the contact angles of all the membrane samples were below 100° and independent of BTO NP content. There was no significant difference between unpolarized and polarized samples (Figure S3c). These results suggest that corona poling treatment does not affect the surface properties of membranes.

Hysteresis loops were observed in the electric field-polarization curves (Figure 2d), indicating the ferroelectric behavior of the nanocomposite membranes. Both maximal polarization (P_m) and residual polarization (P_r) increase with increasing volume fraction of BTO NPs. As a result of the enhanced electric polarization, the BTO NP/P(VDF-TrFE) composite membranes also exhibit substantially increased surface potential with increasing

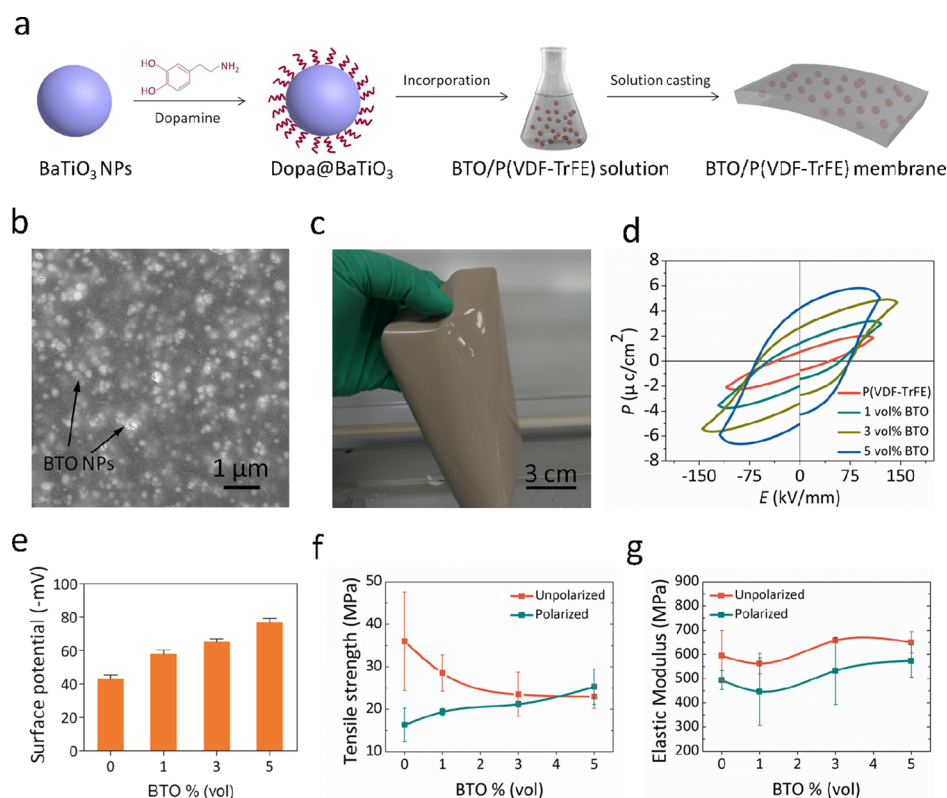


Figure 2. Fabrication and characterizations of BTO NP/P(VDF-TrFE) composite membranes. (a) Schematic diagram of nanocomposite membrane fabrication process. (b) Representative SEM image of nanocomposite membranes. The black arrows denote the BTO NPs. (c) Photograph of the fabricated nanocomposite membrane in bent state, exhibiting flexibility of the membrane. (d) The hysteresis loops of polarized nanocomposite membranes loaded with different BTO NP content of 0, 1, 3, and 5 vol %. (e) The surface potential of polarized nanocomposite membranes after corona poling treatment. (f) Tensile strength and (g) elastic modulus of BTO NP/P(VDF-TrFE) composite membranes before and after corona poling treatment.

amount of BTO NPs (Figure 2e). Interestingly, the highest surface potential of approximately -76.8 mV was obtained for nanocomposite membranes with 5 vol % BTO NPs, which is at the same level as the endogenous potential, which is in the range of -60 to -100 mV.¹³ These results imply that 5 vol % BTO nanocomposite membranes might have the ability to provide the biopotential mimicking microenvironment for cell function and tissue repair.

We note that the high surface potential of the nanocomposite membranes is induced by the synergistic infusion of BTO NPs and P(VDF-TrFE) and the much enhanced interfacial polarization. With a high content of polar β -phase (as indicated by XRD patterns presented in Figure S4), P(VDF-TrFE) exhibits high electrical polarization. Further incorporation of the ferroelectric BTO NPs in the P(VDF-TrFE) matrix induces even higher electrical polarization.¹⁴ More importantly, given the nanometer size of the BTO NPs, the interfaces between BTO NPs and P(VDF-TrFE) take a large volume fraction of the nanocomposites, meaning that the interfacial area is also significantly increased.¹⁵ As the primary electrical polarization mechanism in polymer composites, interfacial polarization, which is proportional to the interfacial area, is greatly enhanced, leading to even higher electrical polarization.^{16,17} So, the surface potential of BTO NP/P(VDF-TrFE) membranes shows a markedly increasing tendency with increasing BTO content.

Considering future clinical application, we then examined the mechanical performance of membranes. Corona poling treatment obviously attenuated the tensile strength of neat P(VDF-TrFE) (Figure 2f), because the electric poling turned

the high-mechanical-performance α -phase to low-mechanical-performance β -phase.¹⁸ The introduction of BTO NPs could help to improve the tensile strength, because the BTO NPs toughen the composite membranes through preventing cracks from propagating. With the combined effects, the membranes with 5 vol % BTO NPs showed a tensile strength of about 25 MPa, which is even higher than that of the unpolarized counterpart. The elastic modulus of all the membrane samples had a moderate reduction after corona poling treatment (Figure 2g). The phenomenon is mainly attributed to the corona poling increasing the degree of crystallinity and the regularity of polymer chain segments in P(VDF-TrFE),¹⁹ which was confirmed by more intense XRD peaks of crystalline phases in polarized samples (Figure S4). But in the BTO NP containing samples, the interface charges derived from corona poling might destroy the molecular link of interface between BTO NP filler and P(VDF-TrFE) matrix, to which is attributed the retention of tensile strength in composite membranes after corona poling treatment.¹⁵ Even so, from the clinical point of view, BTO NP/P(VDF-TrFE) membranes with 5 vol % BTO NP content still have suitable mechanical performance and might be suitable for surgical procedures.

Due to the ability of BTO NP/P(VDF-TrFE) membranes with 5 vol % BTO content to provide artificial microenvironment mimicking physiological biopotential, as well as suitable physicochemical properties, in following work, we focus on the electrical stability and biological function of this kind of nanocomposite membranes.

The electrical stability of polarized BTO NP/P(VDF-TrFE) membranes with 5 vol % BTO content was explored, which might have very important effects on their function realization, especially for tissue defect repair. After immersion in culture medium, the surface potential of polarized nanocomposite membranes exhibited a stable status with more than 60% of original surface potential remaining up to 22 days (Figure 3a). Excellent stability of surface potential of nanocomposite membranes was also present after implantation *in vivo* (Figure 3b). After implantation in a bone

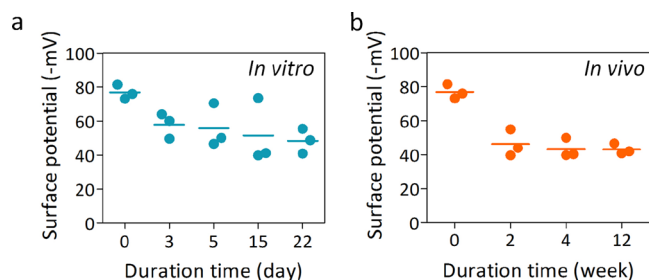


Figure 3. Surface potential change of polarized nanocomposite membranes with 5 vol % BTO NPs during different time periods *in vitro* and *in vivo*: (a) The surface potential of the polarized composite membranes after immersion in serum-free cell culture medium. (b) The surface potential of the polarized nanocomposite membranes after they are implanted into rat calvarial defect region.

defect region for 12 weeks, the surface potential of polarized nanocomposite membranes still remained at 56%, that is, more than half of the original surface potential.

The dramatic stability of surface potential could be attributed to the high residual polarization of the nanocomposite membranes. In principle, the highly disorder interfacial regions between nanometer size BTO NPs and P(VDF-TrFE) matrix are effective traps for space charges, such as ions or free electrons.^{14,20,21} Upon the application of poling electric field, these space charges migrate along the directions of the poling electric field and form large dipoles, giving rise to much enhanced electrical polarization.²² These dipoles switch at a slow rate when the external electric field reverses in direction, resulting in high remnant polarization at the removal of poling electric field. The high remnant polarization renders nanocomposite membranes with sustained retention of surface potential. Sustainable physicochemical properties and surface potential of BTO NP/P(VDF-TrFE) membranes can play a continuous role in maintaining local electric environment and exert long-lasting effects on enhancing bone regeneration.

The biological performance of polarized nanocomposite membranes with 5 vol % BTO content was further investigated. The cytoskeleton observation after 6 h cultivation showed that BM-MSCs on polarized nanocomposite membranes generate most abundant cytoskeleton organization (Figure 4a) and largest cell spreading area (Figure 4g). BM-MSCs were also most enriched in focal adhesion (FA) formation (Figure 4b, g), and

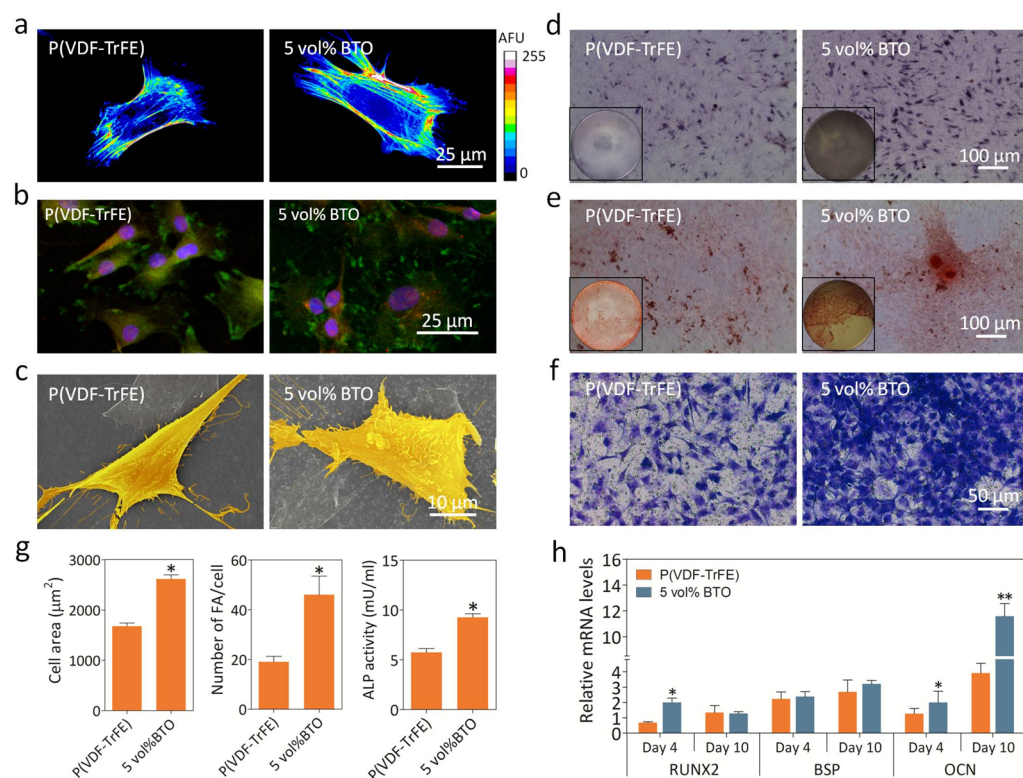


Figure 4. Behavior of BM-MSCs on polarized nanocomposite membranes with 5 vol % BTO content and polarized neat P(VDF-TrFE) membranes. (a) Representative background-subtracted fluorescence images (pseudocolored heat maps) of actin filament organization after 6 h of culture. The fluorescence intensities are scaled by the arbitrary fluorescent unit (AFU). (b) Representative immunofluorescence images of focal adhesions (FAs, green), actin network (phalloidin, red), and nucleus (DAPI, blue) in BM-MSCs cultured for 24 h. (c) Representative SEM images of cell spreading of BM-MSCs cultured for 24 h. (d) Alkaline phosphatase (ALP) activity of BM-MSCs cultured for 7 days. Insets show macroscopic images. (e) Representative Alizarin Red S staining images of BM-MSCs cultured for 21 days. Insets show macroscopic images. (f) Representative images of BM-MSCs migration driven by polarized membranes after coculture for 24 h. (g) Quantitative analysis of cell spreading area, number of focal adhesions per cell, and ALP activity of BM-MSCs on membranes. (h) mRNA expression levels of representative osteogenic genes in BM-MSCs after culture for 4 and 10 days. Error bars represent one standard deviation. (* $p < 0.05$ and ** $p < 0.01$).

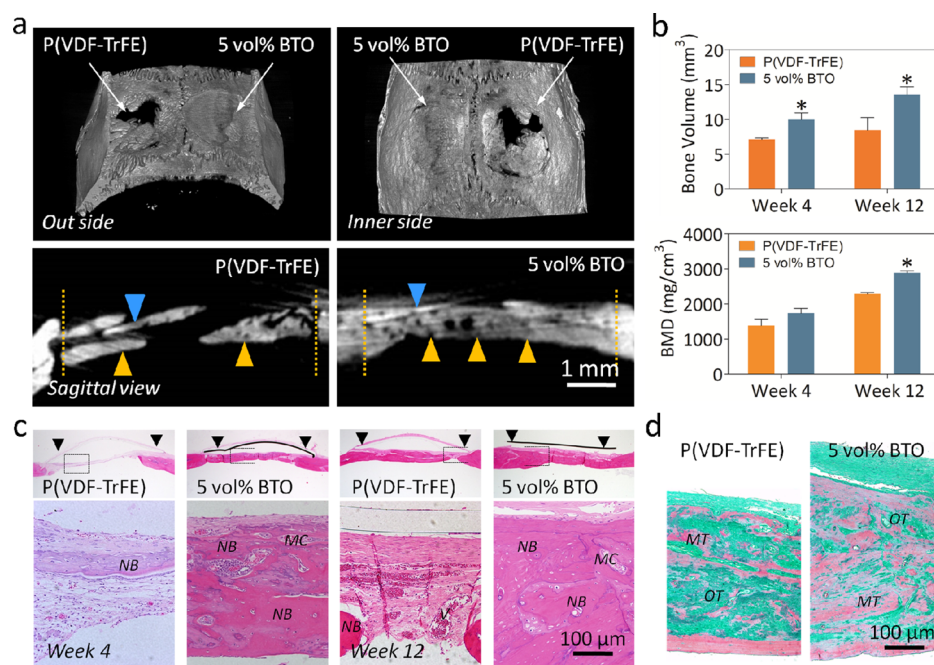


Figure 5. Bone defect repair in rat calvarial models after implantation of polarized nanomembranes with 5 vol % BTO content and polarized neat P(VDF-TrFE) membranes. (a) Representative micro-CT images and sagittal view images of critical-sized rat calvarial full-thickness defects at 12 weeks postimplantation. Blue arrows denote the residual membrane materials. Yellow arrows denote the regenerated new bone. Yellow dotted lines denote the boundary between nascent bone and host bone. (b) Quantitative analysis of bone volume and bone mineral density (BMD) ($*p < 0.05$). (c) H&E staining of histological sections at 4 and 12 weeks after implantation. Black arrows denote the implanted membrane materials. (d) Masson's trichrome staining of histological sections at 12 weeks after implantation (NB, nascent bone; MC, medullary cavity; V, blood vessel; OT, osteoid tissue; MT, mineralized tissue).

exhibited polygonal osteoblastic-like shape with most obvious filopodia (Figure 4c) after 24 h of cultivation on polarized BTO NP/P(VDF-TrFE) membranes with 5 vol % BTO content. Over all, cells on polarized nanocomposite membranes showed increased cell attachment, spreading, and growth in comparison with those on polarized neat P(VDF-TrFE) membranes. These results indicate that polarized nanocomposite membranes induce BM-MSCs behavior improvement. It has been reported that abundant cytoskeleton organization, large cell spreading area, enriched FA formation, and polygonal cell shape with much filopodia are in close relationship with MSCs osteogenic activity.^{23–28}

The osteogenic differentiation of BM-MSCs on membranes was evaluated in terms of ALP activity and mineral deposition in the absence of osteogenic supplements (Figure 4d,e). After incubation for 7 days, apparent ALP positive areas and high ALP activity were detected on polarized 5 vol % BTO nanocomposite membranes (Figure 4d,e and Figure S5a, b). Alizarin Red staining showed that abundant mineralization nodules were induced on polarized 5 vol % BTO nanocomposite membranes and only small mineralization dots were observed on unpolarized 5 vol % BTO NP/P(VDF-TrFE) composite membranes and neat polarized or unpolarized P(VDF-TrFE) samples (Figure 4e, Figure S5a). The quantitative analysis demonstrated highest values of ECM mineralization on polarized 5 vol % BTO nanocomposite membranes (Figure S5c). Osteogenic gene expressions including RUNX-2, BSP, and OCN were further evaluated to investigate osteogenic differentiation of BM-MSCs. Obviously up-regulated gene expression of all the selected genes after 10 days of culture was induced on polarized nanocomposite membranes in the absence of osteogenic supplements (Figure 4h). All these results imply that biopotential mimicking membranes

display excellent osteoinductivity. It could be inferred that harmonious interaction exists between cells and artificial potential microenvironment generated by polarized BTO NP/P(VDF-TrFE) nanocomposite membranes.

To further explore whether the polarized BTO NP/P(VDF-TrFE) membranes with 5 vol % BTO content have direct effect on the recruitment of BM-MSCs, a transwell migration assay *in vitro* was performed. The migration ability of BM-MSCs in polarized nanocomposite membranes was significantly enhanced (Figure 4f). It is considered that MSCs recruitment plays a key role in bone tissue regeneration.^{29–32} MSCs can be recruited by electric microenvironment through galvanotaxis to the defect area and take part in the healing procedure.^{33–35} Our results indicate that the surface potential of polarized 5 vol % BTO NP/P(VDF-TrFE) membranes has a direct recruitment effect on BM-MSCs, which might play an active role in bone defect healing.

To confirm the benefits of artificial physiological electric potential microenvironment on bone defect repair, polarized BTO NP/P(VDF-TrFE) membranes with 5 vol % BTO were implanted covering freshly formed critical-sized calvarial defects in mature rats. Bone growth was evaluated 4 weeks and 12 weeks after implantation. Gross observation displayed conspicuous nascent bone in the defect site after 4 weeks and absolute bone defect healing after 12 weeks for sites covered with polarized nanocomposite membranes, compared with those with either unpolarized nanocomposite membranes (Figure S6a) or polarized P(VDF-TrFE) membranes (Figure S6b). As evidenced by micro-CT detection, the defect was filled with homogeneous and consecutive regenerated mature bone when covered with polarized nanocomposite membranes for 12 weeks (Figure 5a). As expected, micro-CT analysis showed that the polarized

nanocomposite membranes lead to exciting increase in the amount of regenerated bone volume and bone mineral density (BMD) (Figure 5b). As evidenced by X-ray detection, the nascent bone is indistinguishable from the surrounding host bone after 12 weeks implantation of polarized nanocomposite membranes (Figure S7). It is worth noted that the polarized nanocomposite membranes can keep their structure integrity in the period of implantation (Figure S6c). Furthermore, the membrane was not sticky to regenerated new bone tissue. This will be not only beneficial to sustainable maintenance of local electric environment but also convenient for subsequent removal after bone defects heal completely, avoiding inflammation and other side effects resulting from material residual.

Histological analysis revealed that polarized 5 vol % BTO nanocomposite membranes facilitated improved new bone formation within 4 weeks, and newly formed medullary cavity could be observed. After 12 weeks implantation, polarized nanocomposite membranes led to complete healing with flat and consecutive bone-structure formation of full bone maturity. In contrast, in polarized neat P(VDF-TrFE) membranes groups, a small amount of newly formed bone near the margin of the original defect at 4 weeks was observed, and no complete and continuous healing with host tissues appeared when observation time was extended to 12 weeks (Figure 5c). Analysis of Masson's trichrome staining revealed that after 12 weeks implantation of polarized nanocomposite membranes, mature osteoid tissue was present in the top center region of the defect, which is consistent with the assumption that the artificial electric microenvironment encourages new bone formation (Figure 5d). A similar result was also reported that electrostatic fields generated on the surface of Ti implants could promote osteogenesis.³⁶ These results indicate that polarized BTO NP/P(VDF-TrFE) composite membranes can trigger fast bone repair process through sustainable maintenance of electric microenvironment.

CONCLUSION

In this work, the flexible BTO NP/P(VDF-TrFE) nanocomposite membranes were fabricated by utilizing a solution casting method. The introduction of BTO NPs could help to improve the tensile strength of polarized nanocomposite membranes. It is evidenced here that the surface potential of polarized nanocomposite membranes with 5 vol % BTO NPs content reaches to -76.8 mV, which is in the range of natural endogenous biopotential. The surface potential of polarized nanocomposite membranes exhibited a dramatic stability with more than half of original surface potential remained up to 12 weeks when implanted in bone defects. The polarized nanocomposite membranes encouraged osteogenic behavior of BM-MSCs *in vitro* and enhanced fast and extensive bone defect healing through sustainably maintained electric microenvironment *in vivo*. These results suggest that repairing the physiological electric microenvironment contributes to improved bone regeneration outcomes. This might provide an innovative and well-suited strategy for bone regenerative therapies. Taken together with the advantages of excellent flexibility, good applicability and simple fabrication techniques, these nanocomposite membranes would have promising potential for application in bone reconstruction and regeneration.

EXPERIMENTAL PROCEDURES

Fabrication of BTO NP/P(VDF-TrFE) Composite Membranes.

Before BTO NPs were embedded into P(VDF-TrFE) matrix, surface modification of BTO NPs was performed as described in a previous

study.³⁷ Briefly, BTO NPs (99.9%, average particle size of 100 nm, Alfa Aesar) were dispersed by ultrasonic treatment in 0.01 mol/L of dopamine hydrochloride (99%, Alfa Aesar) aqueous solution and stirred for 12 h at 60 °C. For the fabrication of composites, the dopamine-modified BTO NPs and P(VDF-TrFE) (65/35 mol % VDF/TrFE) copolymer powders were proportionally dispersed in *N,N*-dimethylformamide (DMF) by ultrasonication for 2 h, followed by stirring for 12 h, to form a stable suspension. The suspension was then cast into membranes on a special glass substrate and dried at 50 °C for 10 h for solvent volatilizing.

Characterization of Composite Membranes. The surface coatings of BTO NPs were characterized by high-resolution transmission electron microscopy (HR-TEM, JEOL2011) and XPS (PerkinElmer). The morphologies and interstructures of the membranes with different BTO NP content were examined by field emission-scanning electron microscopy (FE-SEM, S-4800, HITACHI, Japan) and X-ray diffraction spectroscopy (XRD, Rigaku D/max 2500 VB2t/PC, Japan). The surface roughness of the membranes was examined by atomic force microscopy (AFM; Auto-Probe CP, Park Scientific Instruments) in the contact mode, and the surface wettability of the samples was assessed by water contact angle measurements performed on a video contact angle instrument (JC2000C1, Shanghai Glory Numeral Technique & Device Co., Ltd., China). The mechanical properties were assessed using a universal mechanical machine (INSTRON-1121, USA).

Electrical Properties Measurement. For the ferroelectric property measurements of the membranes before corona poling, the top copper electrodes with a size of 4 mm diameter were prepared by thermal evaporation. The polarization–electric field (P – E) loops were measured using a commercial ferroelectric analyzer test setup (TF1000, aix ACCT Systems GmbH, Germany) with maximum field amplitude of 4 kV/mm at a frequency of 0.5 Hz. For surface ζ -potential measurements, the membrane samples were first treated by corona poling under DC field of 13 kV at room temperature for 30 min. The surface potential of the polarized membranes was measured using a special surface ζ potential device from Zeta Sizer Nano-ZS Instrument (Malvern Instruments, Worcestershire WR, UK) in an aqueous environment at room temperature. The polarized membrane sample was cut into a rectangle with length of 4 mm and width of 3 mm and glued onto the special bracket. The surface ζ potential measurement was performed according to the manufacturer instructions. For *in vitro* surface potential stability evaluation, the polarized nanocomposite membranes with 5 vol % BTO NPs after immersion in serum-free cell culture medium for 3, 5, 15, and 22 days were rinsed with ddH₂O to evaluate the surface ζ potential. The surface ζ potential value in every kind of membrane was obtained from three samples.

Cell Culture. Rat BM-MSCs (Cyagen Bioscience Inc., Guangzhou, China) were cultured in Dulbecco's modified Eagle medium (DMEM) supplemented with 10% fetal bovine serum (FBS) and 100 IU/mL penicillin–streptomycin. The medium was changed every 2–3 days. At 80–90% confluence, BM-MSCs were detached with 0.25% trypsin/Ethylenediaminetetraacetic acid (EDTA) (Gibco). The cells from 3 to 5 passages were used in the following studies.

Attachment and Spreading of BM-MSCs. BM-MSCs (5×10^4 cells/well) were seeded onto experimental membranes in 12-well plates and incubated at 37 °C in a humidified atmosphere with 5% CO₂. After 6 h of culture, attached cells were fixed with 4% paraformaldehyde, incubated with Alexa Fluor 546-phalloidin (50 μ g/mL) for 1 h and then stained with DAPI for 10 min based on manufacturer's directions. The images were captured by a confocal laser scanning microscopy (Zeiss, CLSM 780, Germany). After 24 h of culture, the samples were fixed in 2.5% glutaraldehyde and serially dehydrated with an increasing ethanol gradient, air-dried in a hood, and sputtered with gold prior to imaging under FE-SEM (S-3000N, Hitachi, Japan) at 20 kV. The cell spreading areas were measured using ImageJ software (National Institutes of Health, Bethesda, MD, USA) employing a random sampling method. For vinculin assay, BM-MSCs were cultured on the membranes in the basic medium, and the samples were harvested after 24 h. Cells were then fixed in 4.0% paraformaldehyde for 15 min at room temperature and washed three times with PBS. Then the cells were permeabilized

with 0.1% Triton X-100 in PBS for 5 min, washed 3 times with PBS, and blocked with 5% bovine serum albumin (BSA) for 1 h. Subsequently, the cells were then incubated with the primary antibody of vinculin (ab18058; Abcam, Inc., diluted 1:200) overnight at 4 °C. After thorough rinsing to remove excess primary antibody, cells were further incubated with the secondary antibody (goat anti-mouse IgG; ab6785; Abcam Inc., diluted 1:1000) for 2 h at ambient temperature. Finally, cells were treated with Alexa Fluor 546-phalloidin (50 $\mu\text{g}/\text{mL}$) for 1 h at room temperature, and then cell nuclei were stained with DAPI for 10 min. Figures of the stained cells were then acquired using CLSM (Carl Zeiss, Jena, Germany). From the fluorescence vinculin staining, the number per cell of the vinculin-positive focal adhesions was measured using MetaMorph software. The measurement was performed for a minimum of 50 cells on each surface.

Cell Migration Assay. BM-MSCs (5×10^4) from passage 4 were loaded into the upper chamber of a 24-well transwell plate (pore size, 8 μm ; Corning, Corning, NY, USA), and 600 μL of DMEM containing 2% FBS was added to the lower chamber where the composite membranes with 10 mm \times 10 mm were plated. After 24 h of coculture, cells on the upper surface of the chamber were removed with a cotton swab. Cells that had migrated to the lower surface of the chamber were fixed with 4% paraformaldehyde, stained for 15 min with 0.5% crystal violet and observed by light microscope (CX21, Olympus, Japan).

Alkaline Phosphatase (ALP) Activity Assay. BM-MSCs/membranes ($n = 3$) were continually cultured in wells. At 7 days, the ALP activity of the adherent cells was assessed using an Alkaline Phosphatase assay kit (Abcam, Cambridge, MA) according to the manufacturer's instructions. The absorbance was measured at a wavelength of 405 nm, and values of ALP activity were read off a standard curve based on standard samples provided by the kit itself.

Alizarin Red S Staining for Mineralization. BM-MSCs/membranes ($n = 3$) were continually cultured in wells. On day 21, the cells grown on the membranes were fixed in 4% paraformaldehyde for 15 min, and then stained in 1% (w/v) Alizarin Red S (pH 4.1–4.5, Sigma-Aldrich) for 2 h at room temperature. After the cells were washed in distilled water three times, images were taken. In the quantitative analysis, the Alizarin Red stain on the specimen was dissolved in 10% cetylpyridinium chloride (Sigma-Aldrich) in 10 mM sodium phosphate to measure the absorbance values at 620 nm.

Quantitative Real-Time PCR Analysis. Total RNA was extracted from each sample using TRIZOL reagent (Gibco-BRL, Gaithersburg, MD) following the manufacturer's instructions. The concentrations of the isolated RNA were determined spectrophotometrically at 260 nm using a NanoDrop ND-2000 spectrophotometer (Thermo Fisher Scientific, Wilmington, DE). The RNA was then reverse transcribed to generate cDNA using the Reverse Transcription system (Promega, Madison, WI). Real-time (RT)-PCR was performed by using SYBR Green detection system with an ABI PRISM 7500 Real-Time PCR system (Applied Biosystems, Foster City, CA). All reactions were carried out in triplicate. The primer sequences of osteogenic genes are listed in Table S1.

Animals and Surgical Procedures. Thirty-six 8-week-old male SD rats were used in this study. The experimental protocol was approved by the Animal Care and Use Committee of Peking University. For establishing the calvarial defect model, the rats were intraperitoneally anesthetized with phenobarbital sodium (100 mg/kg) and the dorsal cranium was exposed. Two critical sized full thickness bone defects (5 mm diameter) were prepared in each rat at the center of each parietal bone using a saline-cooled trephine drill. Each defect was flushed with saline to remove bone debris. The right defects were covered with polarized 5 vol % BTO NPs nanocomposite membranes and the left defects were covered with polarized neat P(VDF-TrFE) membranes or unpolarized 5 vol % BTO NP composite membranes or left empty as control. The whole calvarias were harvested for evaluation after 4 and 12 weeks implantation. For *in vivo* surface potential stability evaluation, the polarized nanocomposite membranes with 5 vol % BTO NPs were taken out from the implantation area after 2, 4, and 12 weeks and rinsed with ddH₂O to remove blood and body fluid. Then the membranes were cut into rectangles with length of 4 mm and width of 3 mm to evaluate

the surface ζ potential with same method as that of membranes soaked in serum-free media.

Micro-CT Scanning Evaluation. At 4 and 12 weeks post-implantation, calvaria samples were harvested and fixed in 4% paraformaldehyde for 24 h at 4 °C, and the specimens were examined using micro-CT scanning as previously described.³⁸ Files were reconstructed using a modified Feldkamp algorithm, which was created using a microtomographic analysis software (Tomo NT; Skyscan, Belgium). After three-dimensional (3D) visualization, bone morphometric analyses, including calculation of bone volume and bone mineral density (BMD) measurements, were carried out on the region of interest (ROI).

Histological Analysis. Tissue processing and sectioning were carried out as our previously described.³⁹ Briefly, tissue samples were fixed in 10% neutral buffered formalin for 7 days, decalcified and dehydrated according to standard protocols, embedded in paraffin, and sectioned at 5 μm thickness. H&E staining and Masson's trichrome staining were performed separately on tissue sections, according to the manufacturer's protocols, and images were captured under light microscope (CX21, Olympus, Japan).

Statistical Analysis. All quantitative data were expressed as mean \pm standard deviation (SD). Statistical analyses were performed using the SPSS 19.0 software (Chicago, IL). Statistical differences were determined using Student's *t* test for independent samples. Differences between groups of * $p < 0.05$ were considered statistically significant and ** $p < 0.01$ was considered highly significant.

ASSOCIATED CONTENT

Supporting Information

The Supporting Information is available free of charge on the ACS Publications website at DOI: 10.1021/acsnano.6b02247.

Characterization of BTO NPs (XRD pattern, HR-TEM images, and XPS spectra), surface characterizations (surface morphology, EDS spectra, surface roughness and water contact angles) and structure characterization (XRD patterns) of nanocomposite membranes, supplementary osteogenic differentiation examination results (alkaline phosphatase staining and Alizarin Red S staining), morphologic observations (macroscopic photographs and X-ray images) of rat calvarial defects repair and the primers sequences utilized for real time RT-PCR (PDF)

AUTHOR INFORMATION

Corresponding Authors

*E-mail: chenlili@whuh.com.

*E-mail: kqdengxuliang@bjmu.edu.cn.

Notes

The authors declare no competing financial interest.

ACKNOWLEDGMENTS

This work was supported by the National Natural Science Foundation of China (Grants 81425007, 31110103905, 51502006), the National Basic Science Research Program (Grant 2012CB933900), and the National High-tech R&D Program of China (Grant 2015AA033601). We thank Liqian Cheng from the Department of Materials Science and Engineering, Tsinghua University, Beijing, China for assistance with ferroelectric property measurements.

REFERENCES

(1) Weaver, J. C.; Astumian, R. D. The Response of Living Cells to Very Weak Electric Fields: the Thermal Noise Limit. *Science* **1990**, *247*, 459–462.

- (2) Burr, H. S.; Northrop, F. S. Evidence for the Existence of an Electro-Dynamic Field in Living Organisms. *Proc. Natl. Acad. Sci. U. S. A.* **1939**, *25*, 284–288.
- (3) Zhao, M.; Song, B.; Pu, J.; Wada, T.; Reid, B.; Tai, G.; Wang, F.; Guo, A.; Walczysko, P.; Gu, Y.; Sasaki, T.; Suzuki, A.; Forrester, J. V.; Bourne, H. R.; Devreotes, P. N.; McCaig, C. D.; Penninger, J. M. Electrical signals Control Wound Healing through Phosphatidylinositol-3-OH Kinase-gamma and PTEN. *Nature* **2006**, *442*, 457–460.
- (4) Huttenlocher, A.; Horwitz, A. R. Wound Healing with Electric Potential. *N. Engl. J. Med.* **2007**, *356*, 303–304.
- (5) Bassett, C. A.; Pawluk, R. J.; Becker, R. O. Effects of Electric Currents on Bone *in Vivo*. *Nature* **1964**, *204*, 652–654.
- (6) Bassett, C. A.; Becker, R. O. Generation of Electric Potentials by Bone in Response to Mechanical Stress. *Science* **1962**, *137*, 1063–4.
- (7) Trumbore, D. C.; Heideger, W. J.; Beach, K. W. Electrical Potential Difference Across Bone Membrane. *Calcif. Tissue Int.* **1980**, *32*, 159–68.
- (8) Song, H. R.; Puri, A.; Lee, J. H.; Park, H. B.; Ra, D. K.; Kim, G. S.; Yeon, S. C. Spontaneous Bone Regeneration in Surgically Induced Bone Defects in Young Rabbits. *J. Pediatr. Orthop. B* **2002**, *11*, 343–349.
- (9) Schmitz, J. P.; Hollinger, J. O. The Critical Size Defect as an Experimental-Model for Craniomandibulofacial Nonunions. *Clin. Orthop. Relat. Res.* **1986**, 299–308.
- (10) Bottino, M. C.; Thomas, V.; Schmidt, G.; Vohra, Y. K.; Chu, T. M. G.; Kowolik, M. J.; Janowski, G. M. Recent Advances in the Development of GTR/GBR Membranes for Periodontal Regeneration-A Materials Perspective. *Dent. Mater.* **2012**, *28*, 703–721.
- (11) Zigman, T.; Davila, S.; Dobric, I.; Antoljak, T.; Augustin, G.; Rajacic, D.; Kovac, T.; Ehrenfreund, T. Intraoperative Measurement of Bone Electrical Potential: A Piece in the Puzzle of Understanding Fracture Healing. *Injury* **2013**, *44*, S16–S19.
- (12) Arbatti, M.; Shan, X. B.; Cheng, Z. Y. Ceramic-polymer Composites with High Dielectric Constant. *Adv. Mater.* **2007**, *19*, 1369–1372.
- (13) Ribeiro, C.; Correia, D. M.; Ribeiro, S.; Sencadas, V.; Botelho, G.; Lanceros-Mendez, S. Piezoelectric Poly(vinylidene fluoride) Microstructure and Poling State in Active Tissue Engineering. *Eng. Life. Sci.* **2015**, *15*, 351–356.
- (14) Zhang, X.; Chen, W.; Wang, J.; Shen, Y.; Gu, L.; Lin, Y.; Nan, C. W. Hierarchical Interfaces Induce High Dielectric Permittivity in Nanocomposites Containing $\text{TiO}_2/\text{BaTiO}_3$ Nanofibers. *Nanoscale* **2014**, *6*, 6701–9.
- (15) Rittigstein, P.; Priestley, R. D.; Broadbelt, L. J.; Torkelson, J. M. Model Polymer Nanocomposites Provide an Understanding of Confinement Effects in Real Nanocomposites. *Nat. Mater.* **2007**, *6*, 278–282.
- (16) Lewis, T. J. Interfaces are the Dominant Feature of Dielectrics at the Nanometric Level. *IEEE Trans. Dielectr. Electr. Insul.* **2004**, *11*, 739–753.
- (17) Lin, X.; Hu, P. H.; Jia, Z. Y.; Gao, S. M. Enhanced Electric Displacement Induces Large Energy Density in Polymer Nanocomposites Containing Core-shell Structured $\text{BaTiO}_3/\text{TiO}_2$ Nanofibers. *J. Mater. Chem. A* **2016**, *4*, 2314–2320.
- (18) Satyanarayana, K. C.; Bolton, K. Molecular Dynamics Simulations of Alpha-to beta-poly(vinylidene fluoride) Phase Change by Stretching and Poling. *Polymer* **2012**, *53*, 2927–2934.
- (19) Wang, Y. F.; Cui, J.; Yuan, Q. B.; Niu, Y. J.; Bai, Y. Y.; Wang, H. Significantly Enhanced Breakdown Strength and Energy Density in Sandwich-Structured Barium Titanate/Poly(vinylidene fluoride) Nanocomposites. *Adv. Mater.* **2015**, *27*, 6658–6663.
- (20) Knauth, P. Inorganic Solid Li ion Conductors: An Overview. *Solid State Ionics* **2009**, *180*, 911–916.
- (21) Zhang, X.; Shen, Y.; Zhang, Q.; Gu, L.; Hu, Y.; Du, J.; Lin, Y.; Nan, C. W. Ultrahigh Energy Density of Polymer Nanocomposites Containing $\text{BaTiO}_3/\text{TiO}_2$ Nanofibers by Atomic-scale Interface Engineering. *Adv. Mater.* **2015**, *27*, 819–24.
- (22) Zhang, X.; Shen, Y.; Xu, B.; Zhang, Q.; Gu, L.; Jiang, J.; Ma, J.; Lin, Y.; Nan, C. W. Giant Energy Density and Improved Discharge Efficiency of Solution-Processed Polymer Nanocomposites for Dielectric Energy Storage. *Adv. Mater.* **2016**, *28*, 2055–2061.
- (23) Liu, W.; Wei, Y.; Zhang, X.; Xu, M.; Yang, X.; Deng, X. Lower Extent but Similar Rhythm of Osteogenic Behavior in hBMSCs Cultured on Nanofibrous Scaffolds *versus* Induced with Osteogenic Supplement. *ACS Nano* **2013**, *7*, 6928–6938.
- (24) Tsimbouri, P. M.; McMurray, R. J.; Burgess, K. V.; Alakpa, E. V.; Reynolds, P. M.; Murawski, K.; Kingham, E.; Oreffo, R. O.; Gadegaard, N.; Dalby, M. J. Using Nanotopography and Metabolomics to Identify Biochemical Effectors of Multipotency. *ACS Nano* **2012**, *6*, 10239–10249.
- (25) Yang, J.; McNamara, L. E.; Gadegaard, N.; Alakpa, E. V.; Burgess, K. V.; Meek, R. M.; Dalby, M. J. Nanotopographical Induction of Osteogenesis through Adhesion, Bone Morphogenic Protein Cosignaling, and Regulation of MicroRNAs. *ACS Nano* **2014**, *8*, 9941–9953.
- (26) Farooque, T. M.; Camp, C. H.; Tison, C. K.; Kumar, G.; Parekh, S. H.; Simon, C. G. Measuring Stem Cell Dimensionality in Tissue Scaffolds. *Biomaterials* **2014**, *35*, 2558–2567.
- (27) Peng, R.; Yao, X.; Ding, J. D. Effect of Cell Anisotropy on Differentiation of Stem Cells on Micropatterned Surfaces through the Controlled Single Cell Adhesion. *Biomaterials* **2011**, *32*, 8048–8057.
- (28) Wang, B.; Cai, Q.; Zhang, S.; Yang, X.; Deng, X. The Effect of Poly(L-lactic acid) Nanofiber Orientation on Osteogenic Responses of Human Osteoblast-like MG63 cells. *J. Mech. Behav. Biomed. Mater.* **2011**, *4*, 600–609.
- (29) Sackstein, R.; Merzaban, J. S.; Cain, D. W.; Dagia, N. M.; Spencer, J. A.; Lin, C. P.; Wohlgemuth, R. *Ex Vivo* Glycan Engineering of CD44 Programs Human Multipotent Mesenchymal Stromal Cell Trafficking to Bone. *Nat. Med.* **2008**, *14*, 181–187.
- (30) Teitelbaum, S. L. Stem Cells and Osteoporosis Therapy. *Cell Stem Cell* **2010**, *7*, 553–554.
- (31) Liu, Y. S.; Ou, M. E.; Liu, H.; Gu, M.; Lv, L. W.; Fan, C.; Chen, T.; Zhao, X. H.; Jin, C. Y.; Zhang, X.; Ding, Y.; Zhou, Y. S. The Effect of Simvastatin on Chemotactic Capability of SDF-1 Alpha and the Promotion of Bone Regeneration. *Biomaterials* **2014**, *35*, 4489–4498.
- (32) Shao, Z. X.; Zhang, X.; Pi, Y. B.; Wang, X. K.; Jia, Z. Q.; Zhu, J. X.; Dai, L. H.; Chen, W. Q.; Yin, L.; Chen, H. F.; Zhou, C. Y.; Ao, Y. F. Polycaprolactone Electrospun Mesh Conjugated with an MSC Affinity Peptide for MSC Homing. *Biomaterials* **2012**, *33*, 3375–3387.
- (33) Zhao, M. Electrical Fields in Wound Healing-An Overriding Signal that Directs Cell Migration. *Semin. Cell Dev. Biol.* **2009**, *20*, 674–682.
- (34) Nakajima, K.; Zhu, K.; Sun, Y. H.; Hegyi, B.; Zeng, Q. L.; Murphy, C. J.; Small, J. V.; Ye, C. I.; Izumiya, Y.; Penninger, J. M.; Zhao, M. KCN15/Kir4.2 Couples with Polyamines to Sense Weak Extracellular Electric Fields in Galvanotaxis. *Nat. Commun.* **2015**, *6*, 8532.
- (35) Sundelacruz, S.; Li, C. M.; Choi, Y. J.; Levin, M.; Kaplan, D. L. Bioelectric Modulation of Wound Healing in a 3D *in Vitro* Model of Tissue-Engineered Bone. *Biomaterials* **2013**, *34*, 6695–6705.
- (36) Ning, C.; Yu, P.; Zhu, Y.; Yao, M.; Zhu, X.; Wang, X.; Lin, Z.; Li, W.; Wang, S.; Tan, G.; Zhang, Y.; Wang, Y.; Mao, C. Built-in Microscale Electrostatic Fields Induced by Anatase-rutile-phase Transition in Selective Areas Promote Osteogenesis. *NPG Asia Mater.* **2016**, *8*, e243.
- (37) Hu, P. H.; Shen, Y.; Guan, Y. H.; Zhang, X. H.; Lin, Y. H.; Zhang, Q. M.; Nan, C. W. Topological-Structure Modulated Polymer Nanocomposites Exhibiting Highly Enhanced Dielectric Strength and Energy Density. *Adv. Funct. Mater.* **2014**, *24*, 3172–3178.
- (38) Zhang, X. H.; Xu, M. M.; Song, L.; Wei, Y.; Lin, Y. H.; Liu, W. T.; Heng, B. C.; Peng, H.; Wang, Y.; Deng, X. L. Effects of Compatibility of Deproteinized Antler Cancellous Bone with Various Bioactive Factors on their Osteogenic Potential. *Biomaterials* **2013**, *34*, 9103–9114.
- (39) Meng, S.; Zhang, X.; Xu, M.; Heng, B. C.; Dai, X.; Mo, X.; Wei, J.; Wei, Y.; Deng, X. Effects of Deer Age on the Physicochemical Properties of Deproteinized Antler Cancellous Bone: An Approach to Optimize Osteoconductivity of Bone Graft. *Biomed. Mater.* **2015**, *10*, 035006.